

Theoretical study of a passively mode-locked integrated laser based on transition-metal dichalcogenides and graphene

Dimitrios Chatzidimitriou ^{*}, Georgios Nousios , Thomas Christopoulos , and Emmanouil E. Kriezis 

School of Electrical and Computer Engineering, Aristotle University of Thessaloniki, Egnatia Street, University Campus, 54124, Thessaloniki, Greece

 (Received 8 October 2023; revised 26 February 2024; accepted 28 March 2024; published 19 April 2024)

We assess the theoretical performance of a mode-locked silicon-rich-nitride ring laser, which is partly overlaid with a MoS₂/WSe₂ bilayer and partly with a graphene monolayer. Through an external vertical optical pump at 740 nm, the transition-metal dichalcogenide (TMD) bilayer can be inverted and provide gain at 1128 nm while the graphene monolayer acts as the fast broadband saturable absorber. We show that under modest pumping conditions, we can reach a stable mode-locked regime that can deliver on-chip pulsed output with milliwatt peak power and down to 400 fs in duration. The ring laser is studied by rigorously modeling the TMD bilayer as a semiclassical three-level system and incorporating the resulting resonant polarization to the nonlinear Schrödinger equation (NLSE). Within the NLSE formalism we are able to also incorporate material and waveguide dispersion as well as the significant Kerr-type nonlinearity of the silicon-rich-nitride waveguide. Furthermore, we discuss all the necessary physical and mathematical approximations needed to numerically solve the propagation problem, based on an implementation of the split-step Fourier method with the atomic polarization term. Our mathematical treatment is very general and can be adapted to any two-dimensional-material-enhanced traveling wave source. Finally, this work shows the feasibility and potential of TMD bilayers as well as graphene for the development of efficient integrated pulsed on-chip sources.

DOI: [10.1103/PhysRevA.109.043522](https://doi.org/10.1103/PhysRevA.109.043522)

I. INTRODUCTION

Two-dimensional (2D) materials are a major research topic of the photonic literature, spanning both passive and active applications, such as signal modulators, nonlinear elements, saturable absorbers, photodetectors, and light sources [1–3]. Their success is owed to their excellent optical properties (electrically controllable absorption, high nonlinear index, and high carrier mobility and broadband response) and to their compatibility with silicon-on-insulator and the more recent silicon-rich-nitride (SRN) platforms [4–6].

On-chip light sources are highly desirable in both industry and research. With silicon being an indirect band-gap semiconductor, the conventional approach through hybrid integration with III-V semiconductors still poses technological challenges due to the silicon lattice mismatch [7,8]. Alternatively, rare-earth-doped waveguides have been fabricated [9–11], as well as SRN waveguides enclosed by polymers with organic-dye molecules. The latter, though, suffer from the photobleaching effect [12] which inhibits high repetition rates [13,14]. Graphene, black phosphorous, hexagonal boron nitride, and transition-metal dichalcogenides (TMDs) have all been considered as 2D alternatives [3,8]. Specifically, TMDs are direct band-gap semiconductors and have been used in lasing demonstrations in the near-infrared (NIR) and visible spectral regions [15,16]. More intriguing, yet,

are TMD bilayer heterostructures which offer slower radiative recombination rates and electrostatically tunable emission wavelengths [17,18]. Therefore, TMD heterostructures are a promising candidate for the realization of efficient integrated laser sources in the NIR region [19–22].

In this article, we theoretically investigate an NIR mode-locked integrated laser, with the fundamental building blocks realized by 2D materials, i.e., the gain and the saturable absorption (SA). The photonic source is a ring resonator that consists of a wire SRN waveguide on a silicon oxide substrate. SRN is chosen due to the expanded transparency window and the absence of the two-photon absorption effect, and the wire waveguide archetype is chosen due to its high light-matter interaction with the considered 2D materials. Gain is introduced by a MoS₂/WSe₂ bilayer overlaying a quadrant of the ring. The heterostructure is optically pumped by an external vertical source at 740 nm and emits light at 1128 nm. The fast and broadband saturable absorber is implemented by a graphene monolayer occupying a length of a few microns. This small loss-modulation is enough to passively mode lock the laser. Due to the millimeter length of the cavity, the ring resonator cannot be described as a point with the coupled-mode theory [19,23]; instead, we need to spatially propagate a time-varying field. Thus, we employ the nonlinear Schrödinger equation (NLSE) coupled with a semiclassical three-level system to describe the gain mechanism of the bilayer. We rigorously show how the rate equations are fitted into the NLSE, and we numerically demonstrate the stable mode-locked operation for very modest pumping conditions.

^{*}dchatzid@auth.gr

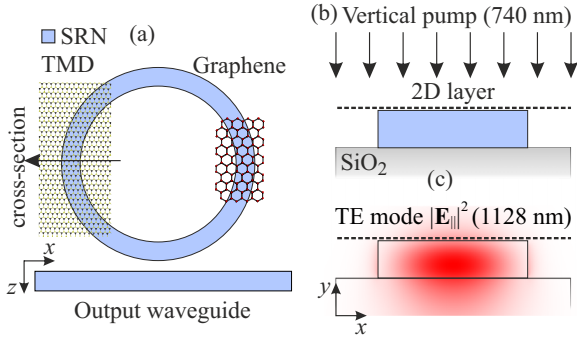


FIG. 1. (a) Top-down view of the SRN ring resonator overlaid with a MoSe₂/WSe₂ bilayer and a graphene monolayer (not to scale). The arrow shows the slice of the cross section. (b) SRN wire waveguide cross section with vertical external optical pump direction (plane wave). (c) Parallel to the 2D material electric-field distribution $|E_{||}|^2$ of the TE-supported mode.

II. DESCRIPTION OF THE RING LASER

The ring laser is shown in Figs. 1(a) and 1(b). SRN and silica have a refractive index of $n_{\text{SRN}} = 2.0089$ and $n_{\text{SiO}_2} = 1.45$, respectively, at $\lambda_0 = 1128$ nm. The height and the width of the waveguide are 150 nm, and 1.2 μm , respectively. The graphene linear surface conductivity is $60 \mu\text{S}$ [24]. The total linear surface conductivity of MoS₂/WSe₂ is $i369 \mu\text{S}$, equal to the sum of each layer's surface conductivity, as if light successively passes through each layer [25,26]. This conductivity only accounts for the dielectric properties of the bilayer at 1128 nm. The frequency dispersion of each material is included through the respective Sellmeier relations. The laser is assumed to be air-clad. Out-coupling is performed with a side-coupled bus waveguide (80:20 coupler). Linear losses (including losses from wall corrugations and radiative losses) are taken to be 1 dB/mm and are included heuristically as a perturbation to the linear solution.

The geometric dimensions of the waveguide were designed firstly to provide high interaction between the 2D materials and the guided mode so that a significant portion of the field is guided close to the top 2D layer, and secondly, to ensure single (cross-sectional) mode operation. The two possible mode polarizations that we could choose from are the TE (dominant electric field component parallel to the 2D layer) and TM (dominant electric field component normal to the 2D layer). The interaction of the 2D materials considered here (graphene monolayer and MoS₂/WSe₂ bilayer) with an electromagnetic field is described through a surface current density or an equivalent surface polarization, and only field components which are tangent to the surface of the 2D material can interact with it. Note, that the response of these 2D materials is considered to be isotropic for fields tangent to their surface. In our design, the 2D materials lie on the x - z plane, which means that the maximum interaction will be provided by fields strongly polarized in any of these directions. The TE mode interacts with the 2D materials through its x component. The TM mode interacts through its z component, and in some cases, e.g., in a silicon platform, can provide a better overlap compared to the TE mode [27]. The SRN waveguide, though, does not have as strong a refractive index contrast as an Si waveguide,

and thus the z component of the TM mode provides a weaker overlap than the x component of the TE mode. Consequently, the waveguide is engineered to only support a single TE mode for the wavelengths considered.

From a cross-sectional finite element method (FEM) modal analysis, the TE mode has an $n_{\text{eff}} = 1.4798$ and the field distribution can be seen in Fig. 1(c). The perimeter of the ring is $L_r = 4$ μm , from which the TMD bilayer covers 1 μm and the graphene section just 20 μm . The cold cavity axial mode separation is calculated to be $v_g/L_r \approx 41.22$ GHz in the vicinity of 1128 nm, with v_g being the group velocity.

Finally, we would like to note that we have assumed that 2D materials lie directly on top of the photonic component without any bonding. This has been shown to be experimentally feasible in a number of demonstrations, such as in Refs. [7,20,21,28]. Also, although our theoretical work assumes the material to be in absolute contact with the waveguide, thus maximizing light-matter interaction, slight deviations of some nanometers (e.g., the 2D material is moved 10 nm away from the waveguide) will lead to very small quantitative differences from the results presented.

III. METHODS: THEORETICAL MODELING OF THE RING LASER

Optical pumping happens between the valence and conduction band of the WSe₂ layer, which has a transition energy of 1.675 eV (or 740 nm). The photoexcited carriers either relax back to the WSe₂ valence band or, due to the type-II band alignment of the heterostructure, to the conduction band of the MoS₂ layer. The former path has a total relaxation lifetime of a few picosecond, whereas the latter has an ultrafast lifetime of 1–100 fs [29]. Due to the considerable difference in relaxation times, the intralayer relaxation (radiative and nonradiative) can be safely neglected. From the MoS₂ conduction band, carriers relax back into the WSe₂ valence band (the transition energy is 1.1 eV or 1128 nm) with a relaxation lifetime of 1 ns [17]. From reported values, the spontaneous emission lifetime is also close to 1 ns [15,20,30], so we ignore any nonradiative relaxation and assume that the total energy decay rate equals the radiative one. Consequently, the TMD heterostructure is modeled as a three-level system, with level 0 being the WSe₂ valence band, level 2 the WSe₂ conduction band, and level 1 the MoS₂ conduction band.

We consider the TE mode propagating in the ring laser, whose slowly varying envelope A is centered around ω_0 . The NLSE in the region of the TMD bilayer is [31]

$$\frac{\partial A(z, T)}{\partial z} = \sum_{m=2}^3 \frac{i^{m+1}}{m!} \beta_m \frac{\partial^m}{\partial T^m} A + i\gamma |A|^2 A + \frac{\alpha}{2} A + \frac{i\omega_0}{4\sqrt{E_n}} e^{-i\beta_0 z} \iint_S \mathbf{e}^* \cdot \mathbf{P}(\mathbf{r}, T) dS, \quad (1)$$

where $\beta_m = d\beta^m/d\omega^m$ evaluated at ω_0 , β_0 is the propagation constant at ω_0 , γ is the total Kerr nonlinear parameter from all materials excluding the bilayer, and α is the linear power loss coefficient from all sources, again excluding the bilayer. The integral in Eq. (1) is over the waveguide transverse cross section S . The equation is written in the moving time-frame

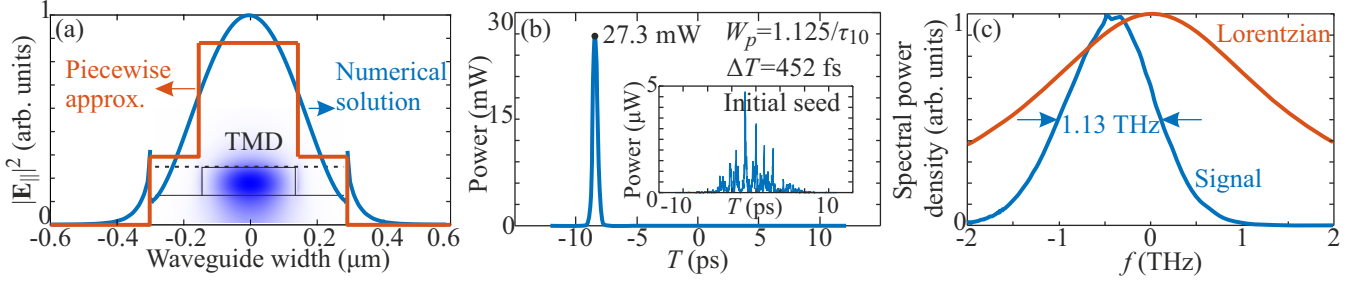


FIG. 2. (a) Blue curve: $|\mathbf{e}_{\parallel}|^2$ distribution on the TMD layer, evaluated by the FEM mode solver. Red curve: Piecewise approximation of $|\mathbf{e}_{\parallel}|^2$, where each segment is calculated as the mean of the respective true field distribution. Inset: Cross-sectional $|\mathbf{e}_{\parallel}|^2$ in the waveguide. The position of the TMD bilayer is shown with a dashed black line. (b) Circulating power of the stable Gaussian-like pulse. The inset shows the initial random noise seed. (c) Spectral power density of the circulating pulse. The red curve is a reference Lorentzian distribution normalized to the maximum spectral density of the signal and with the same bandwidth as that of the signal transition (20 Trad/s).

T with velocity equal to the group velocity $v_g = d\omega/d\beta$. The real quasimonochromatic electric field is given by

$$\mathcal{E}(\mathbf{r}, t) = \frac{1}{2}[\mathbf{E}(\mathbf{r}, t)e^{-i\omega_0 t} + \text{c.c.}], \quad (2a)$$

$$\mathbf{E}(\mathbf{r}, t) = A(z, t) \frac{\mathbf{e}(x, y, \omega_0)}{\sqrt{E_n}} e^{i\beta_0 z}, \quad (2b)$$

$$E_n = \frac{1}{2} \left| \iint_S \mathbf{e} \times \mathbf{h}^* \cdot \hat{\mathbf{z}} dS \right|. \quad (2c)$$

Note that A contains all dispersion and nonlinear effects that act on the unperturbed fields \mathbf{e} and \mathbf{h} at ω_0 . The unperturbed mode profile is evaluated with the COMSOL MULTIPHYSICS FEM mode solver. The dielectric effects of the bilayer are accounted for through its purely imaginary surface conductivity by modeling the layer as a surface-current density boundary condition.

The term in the second line of Eq. (1) contains the effect of the active medium on propagation, which is considered a perturbation to the linear solution, i.e., does not significantly change the mode field profiles and propagation constants. We define the projection of the active medium polarization onto the guided mode as

$$p(z, T) = e^{-i\beta_0 z} \iint_S \frac{\mathbf{e}^*}{\sqrt{E_n}} \cdot \mathbf{P}(\mathbf{r}, T) dS. \quad (3)$$

The real polarization field, similar to Eq. (2a), is given by

$$\mathcal{P}(\mathbf{r}, t) = \frac{1}{2}[\mathbf{P}(\mathbf{r}, t)e^{-i\omega_0 t} + \text{c.c.}], \quad (4a)$$

$$\mathbf{P}(\mathbf{r}, t) = \mathbf{P}_{\text{TMD}}(\mathbf{r}, t) e^{i\beta_0 z} \delta(\mathbf{r} - \mathbf{r}_{\text{TMD}}), \quad (4b)$$

where we have retained only polarization terms that are in-phase with the guided mode. The surface polarization produced by a 2D material is zero outside the 2D layer, indicated by the delta function $\delta(\mathbf{r} - \mathbf{r}_{\text{TMD}})$ (with units 1/m), where \mathbf{r}_{TMD} is a position vector to any point on the TMD surface. Thus, all surface integrals on the waveguide cross section are simplified to line integrals: Eq. (3) becomes

$$p(z, T) = \int_{\text{TMD}} \frac{\mathbf{e}^*}{\sqrt{E_n}} \cdot \mathbf{P}_{\text{TMD}}(\mathbf{r}, T) d\ell, \quad (5)$$

where the integration is carried over the curve that results from the intersection of the transverse cross section S and the surface of the TMD [the dashed lines in Figs. 2(b) and 2(c)].

Modeling the TMD bilayer as a three-level system with a homogeneously broadened Lorentzian line shape and using the Slowly Varying Envelope Approximation (SVEA) implied by Eq. (4a), the rate equations for the resonant atomic transitions are given by [32,33]

$$\frac{dN_0}{dt} = -W_p(N_0 - N_2) + \frac{1}{\tau_{10}}N_1 + \frac{1}{2\hbar}\text{Im}\{\mathbf{E} \cdot \mathbf{P}^*\}, \quad (6a)$$

$$\frac{dN_1}{dt} = -\frac{1}{\tau_{10}}N_1 + \frac{1}{\tau_{21}}N_2 - \frac{1}{2\hbar}\text{Im}\{\mathbf{E} \cdot \mathbf{P}^*\}, \quad (6b)$$

$$\frac{dN_2}{dt} = W_p(N_0 - N_2) - \frac{1}{\tau_{21}}N_2, \quad (6c)$$

$$\frac{d\mathbf{P}}{dt} = -\frac{1}{T_2}(1 - i\delta)\mathbf{P} + i\frac{\tilde{K}\Delta N_{10}}{2\omega_0}\mathbf{E}, \quad (7)$$

where N_i are the surface carrier densities (in m^{-2}) of the i th level, W_p is the stimulated probability of the 2-0 pump transition, $\tau_{21} = 100$ fs is the (nonradiative) energy relaxation time between levels 2 and 1, $\tau_{10} = 1$ ns is the total energy relaxation lifetime for the 1-0 signal transition, $T_2 = 2/\Delta\omega_\alpha$ is the polarization dephasing time for the signal transition, $\Delta\omega_\alpha = 20$ Trad/s [34] is the full width at half maximum (FWHM) bandwidth of the signal resonant atomic transition, $\delta = (\omega_0^2 - \omega_\alpha^2)/2\omega_0$, ω_α is the midband signal transition frequency, \tilde{K} is a tensor coupling constant, and finally, $\Delta N_{10} = N_1 - N_0$ is the population difference, without degeneracies, at the signal transition.

A. Polarization equation of motion

An “isotropic” response of a 2D material, located in the x - z plane, that does not interact with field components normal to its surface leads to a coupling constant that is given by [32]

$$\tilde{K} = \frac{\omega_0 \epsilon_0 \gamma_{\text{rad}} \lambda_0^3}{4\pi^2 n_h} \times \frac{3}{2} \begin{bmatrix} 1 & 0 & 0 \\ 0 & 0 & 0 \\ 0 & 0 & 1 \end{bmatrix}. \quad (8)$$

In Eq. (8), λ_0 is the signal wavelength in vacuum, n_h is the refractive index of the host material (i.e., extracted from the nonresonant dielectric properties of the TMD bilayer), and finally, γ_{rad} is the radiative energy decay rate. From the published literature the exact value of the radiative decay rate is not yet clear [15,16,30]. Here, we adopt the assumption that

the nonradiative decay rate is much smaller than the radiative one, which effectively means that the total energy decay rate $\gamma_{\text{tot}} = \gamma_{\text{rad}} + \gamma_{\text{nr}} \approx \gamma_{\text{rad}}$ and thus $\gamma_{\text{rad}} \approx 1/\tau_{10}$.

With Eq. (8), we can substitute $\tilde{K}\mathbf{E} = K\mathbf{E}_{\parallel}$ in Eq. (7), where \mathbf{E}_{\parallel} is the tangential to the 2D material electric field. The now scalar K has absorbed the 3/2 factor and is given by

$$K = \frac{3}{2} \frac{\omega_0 \epsilon_0 \gamma_{\text{rad}} \lambda_0^3}{4\pi^2 n_h}. \quad (9)$$

We now take the dot product of Eq. (7) with $e^{-i\beta_0 z} \mathbf{e}^* / \sqrt{E_n}$, integrate over the entire cross section of the waveguide, and use the definition of Eq. (5), which leads to

$$\frac{dp}{dt} = -\frac{1}{T_2} (1 - i\delta)p + i \frac{K}{2\omega_0 E_n} \int_{\text{TMD}} \Delta N_{10} |\mathbf{e}_{\parallel}|^2 d\ell A. \quad (10)$$

Equation (10) is exact, within the approximations and assumptions made so far, but the integral on the right-hand side complicates the solution. To this end, we make a piecewise approximation of $|\mathbf{e}_{\parallel}|^2$, where in each segment with length L_j of the TMD layer (in the cross section) the field distribution is assumed constant and equal to its mean value $|\mathbf{e}_{\parallel}^{(j)}|^2 = \text{const} = \frac{1}{L_j} \int_{L_j} |\mathbf{e}_{\parallel}|^2 d\ell$.

Figure 2(a) shows how the field profile in the ring laser is approximated for the carrier-rate equations. Based on the field approximation, instead of integrating on the whole cross section to derive Eq. (10), we dot multiply with the electric field mode and integrate Eq. (7) over the specific intervals L_j so we get an equal number of equations

$$\frac{dp^{(j)}}{dt} = -\frac{1}{T_2} (1 - i\delta)p^{(j)} + i \frac{K |\mathbf{e}_{\parallel}^{(j)}|^2 L_j}{2\omega_0 E_n} \Delta N_{10}^{(j)} A, \quad (11)$$

where $N_i^{(j)}(z, t) = \frac{1}{L_j} \int_{L_j} N_i(\mathbf{r}, t) d\ell$. Naturally the total polarization projection of Eq. (5) is $\Sigma_j p^{(j)}$.

B. Carrier equations

Returning to the carrier-rate equations, Eq. (6) are integrated over the various segments L_j and written as

$$\frac{dN_0^{(j)}}{dt} = -W_p(N_0^{(j)} - N_2^{(j)}) + \frac{1}{\tau_{10}} N_1^{(j)} + \frac{\text{Im}\{Ap^{(j)*}\}}{2\hbar L_j}, \quad (12a)$$

$$\frac{dN_1^{(j)}}{dt} = -\frac{1}{\tau_{10}} N_1^{(j)} + \frac{1}{\tau_{21}} N_2^{(j)} - \frac{\text{Im}\{Ap^{(j)*}\}}{2\hbar L_j}, \quad (12b)$$

$$\frac{dN_2^{(j)}}{dt} = W_p(N_0^{(j)} - N_2^{(j)}) - \frac{1}{\tau_{21}} N_2^{(j)}. \quad (12c)$$

A simplification of Eq. (12) is to assume that carriers flow out of level 2 much faster than they are pumped, $1/\tau_{21} \gg W_p$, and that Eq. (12c) is at the steady state $dN_2^{(j)}/dt = 0$, which leads to $N_2^{(j)}/\tau_{21} \approx W_p N_0^{(j)}$. By also using the carrier conservation $N_{\text{tot}}^{(j)} = N_0^{(j)} + N_1^{(j)} = N_{\text{tot}}$ (N_{tot} being the constant total carrier density), we can reduce Eq. (12) to a single well-known differential equation for the population difference:

$$\frac{d\Delta N_{10}^{(j)}}{dt} = \frac{\Delta N_{10}^{(j)} - \Delta N_{10}^{(j)}}{T_1} + \frac{1}{\hbar L_j} \text{Im}\{Ap^{(j)*}\}, \quad (13)$$

where $\Delta N_{10}^{(j)} = -\frac{W_p - 1/\tau_{10}}{W_p + 1/\tau_{10}} N_{\text{tot}}$ and $T_1 = W_p + 1/\tau_{10}$. The population inversion threshold for the pump is simply $W_{p,\text{th}} = 1/\tau_{10}$.

C. Graphene SA

Regarding the graphene section, SA is taken into account by including an SA term in the NLSE:

$$\frac{\partial A(z, T)}{\partial z} = \sum_{m=2}^3 \frac{i^{m+1}}{m!} \beta_m \frac{\partial^m}{\partial T^m} A + i\gamma |A|^2 A + \frac{\alpha}{2} A + \frac{1}{2} \frac{\alpha_{\text{sat}}}{1 + |A|^2/A_{\text{sat}}^2} A, \quad (14)$$

where $\alpha_{\text{sat}} = \frac{\sigma_{\text{gr}}}{4\sqrt{E_n}} \int |\mathbf{e}|^2 d\ell$ [31] is the saturable-power-loss coefficient of graphene (the integration is carried over the total graphene length in the cross section), calculated to be approximately 0.1 dB/ μm assuming that all of graphene's induced losses can be saturated. The saturation power A_{sat}^2 is found to be about 10.1 mW, calculated according to the procedure for relative long pulses prescribed in Ref. [31]. Note that Eq. (14) implies that the SA action is instantaneous, an approximation which we employ since graphene dynamics are much faster (in the picosecond regime) [31] compared to the TMD gain dynamics [18,20,29]. Furthermore, Eq. (14) only applies to the portion of the ring overlaid with graphene. Furthermore, the nonlinear parameter γ must also take into account the Kerr contribution from graphene which is found to be $-147 \text{ W}^{-1} \text{ m}^{-1}$ (self-defocusing), assuming a third-order nonlinear conductivity of $i1.14 \times 10^{-21} \text{ Sm}^2/\text{V}^2$ [31]. The Kerr contribution from SRN to the nonlinear parameter is found to be $254 \text{ W}^{-1} \text{ m}^{-1}$ (self-focusing), assuming a nonlinear index $n_2 = 2.8 \times 10^{-17} \text{ m}^2/\text{W}$ [35]. Thus, the total nonlinear parameter for the waveguide section overlaid with graphene is reduced to $107 \text{ W}^{-1} \text{ m}^{-1}$.

D. Numerical solution

The final system of equations that describe the propagation of a quasimonochromatic single-mode field in a waveguide with TMD bilayer consists of Eqs. (1), (11), and (13). For an easier reference, all these equations are repeated below:

$$\frac{\partial A(z, T)}{\partial z} = \sum_{m=2}^3 \frac{i^{m+1}}{m!} \beta_m \frac{\partial^m}{\partial T^m} A + i\gamma |A|^2 A + \frac{\alpha}{2} A + \frac{i\omega_0}{4} \sum_j p_j, \quad (15a)$$

$$\frac{dp_j}{dt} = -\frac{1}{T_2} (1 - i\delta)p_j + i \frac{K |\mathbf{e}_{\parallel}^{(j)}|^2}{2\omega_0 E_n} \Delta N_{10}^{(j)} A, \quad (15b)$$

$$\frac{d\Delta N_{10}^{(j)}}{dt} = \frac{\Delta N_{10}^{(j)} - \Delta N_{10}^{(j)}}{T_1} + \frac{1}{\hbar} \text{Im}\{Ap_j^*\}, \quad (15c)$$

and we also summarize in Table I the values of the physical quantities used in our simulations.

The solution of the appropriate NLSE, Eq. (14) for the graphene section or Eq. (15) for the TMD section, is carried out with the widely adopted split-step Fourier (SSF) method. With the SSF method, the field is propagated for a single

TABLE I. Summary of the values of geometrical and physical variables used in the simulations.

Signal/lasing wavelength λ_0	1128	nm
Pump wavelength λ_p	740	nm
SRN refractive index n_{SRN}	2.0089	
Silica refractive index n_{SiO_2}	1.45	
Waveguide height	150	nm
Waveguide width	1.2	μm
Ring perimeter	4	mm
Waveguide linear losses α	1	dB/mm
Graphene surface conductivity	60	μS
SA saturation power A_{sat}^2	10.1	mW
MoS ₂ /WSe ₂ surface conductivity	$i369$	μS
SRN nonlinear index n_2	$i2.8 \times 10^{-17}$	m^2/W
Graphene coverage	20	μm
TMD coverage	1	mm
TE mode effective index n_{eff}	1.4798	
Group velocity v_g^a	1.6488×10^8	m/s
GVD dispersion β_2^a	1.6162×10^{-24}	s^2/m
Third-order dispersion β_3^a	-4.0366×10^{-39}	s^3/m
γ in graphene region	107	$\text{W}^{-1} \text{m}^{-1}$
γ outside graphene region	254	$\text{W}^{-1} \text{m}^{-1}$
Relaxation lifetime τ_{21}	100	fs
Relaxation lifetime τ_{10}	1	ns
FWHM bandwidth $\Delta\omega_\alpha$	20	Trad/s

^aCalculated in the absence of 2D materials.

round trip and then used as the input for the next round trip. Thus, for the m th round trip

$$A_m(0, T) = A_{m-1}(L_r, T), \quad (16)$$

with L_r being the perimeter of the ring laser.

The spatial propagation for a length Δz (we keep the letter z since it is common in the NLSE formalism, but in reality z is the arc length) is carried out in three steps: first the linear operator acts in the spectral domain, containing all dispersion effects. Then, if present, we take into account the active medium:

$$A(z + \Delta z, T) = A(z, T) + \Delta z \left(\frac{i\omega_0}{4} \sum_j p_j \right), \quad (17)$$

where p_j is evaluated by numerically solving (with a Runge-Kutta method) the initial value problem of Eqs. (15b) and (15c) and with initial carrier distributions given by $\Delta N_m^{(j)}(z, -T_r/2) = \Delta N_{m-1}^{(j)}(z, T_r/2)$. To have access to the latter initial condition, the carrier distributions of the previous round trip at $T_r/2$ and at every z must be saved. Also, due to the time and field dependence of the carrier distributions, the width of the time window must be chosen to be exactly equal to the round trip time $T_r = L_r/v_g$. Finally, to complete the Δz propagation, the nonlinear operator containing the Kerr effect is applied in the time domain. Note that depending on the position on the ring circumference, the underlying NLSE being solved is modified. For the graphene section, we use Eq. (14) and thus take into account graphene SA and the Kerr nonlinearity from SRN and graphene (adding the individual γ parameters). For the TMD section, we use Eqs. (15), where we take into account the TMD polarization and the SRN Kerr

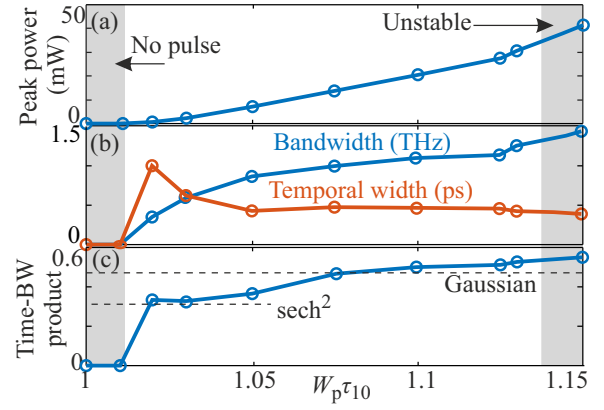


FIG. 3. (a) Circulating pulse peak power in mW, (b) temporal (ps) and spectral (THz) FWHM width, and (c) time-bandwidth product of the stable pulse formed after around 600 round trips versus the normalized pumping rate $W_p \tau_{10}$.

nonlinearity. For the section where neither graphene nor TMD is present, the NLSE takes the form of Eq. (14) without the SA term and assigning to γ the SRN Kerr contribution.

The most expensive, computationally, step is the solution of the carrier and polarization equations. Note though, that in the SSF carrier density advancement step, the electric field is considered constant. Thus, in the absence of spatial derivatives (diffusion), the equations' sets of the various segments L_i are decoupled and can be solved in parallel. Due to the symmetry of the electric field, see Fig. 2, we used two segments for the piecewise approximation.

On a final note, if there are no significant changes over one round trip, Eq. (15a) can be averaged over a round trip and with the help of Eq. (16) transformed to the Lugiato-Lefever equation [36].

IV. MODE-LOCKED OPERATION AND DISCUSSION

From the simulation results, in Fig. 2(b) we show the circulating optical power in the ring laser, during the 600th round trip, calculated for an 80:20 output coupler. Thus, the available output power will be about 20% of the 27 mW shown, which is more than adequate for a variety of applications. Figure 2(c) shows the corresponding spectrum, centered at ω_0 . This pulse was formed out of an initial noisy input that is added at the start of each round trip (inset), which simulates the effect of spontaneous emission in the given propagation direction. The noise distribution is generated in the frequency domain by randomizing the phase of the spectral components of a Lorentzian distribution of the same bandwidth as that of the TMD signal interlayer transition. The mean noise power was chosen heuristically and is of the order of 0.1 μW . You can also observe in the inset of Fig. 2(b) that the initial noisy seed passes through a Gaussian window to avoid energy reaching the edges of the temporal window.

In this specific example, with the pumping rate $W_p = 1.125/\tau_{10}$, we observe a stable Gaussian-like pulse being formed with 27.3-mW peak power and a FWHM duration of 452 fs. Figure 3(a) shows the peak power, Fig. 3(b) shows the 3-dB bandwidth and the temporal width, and Fig. 3(c) shows the time-bandwidth product versus the pumping parameter

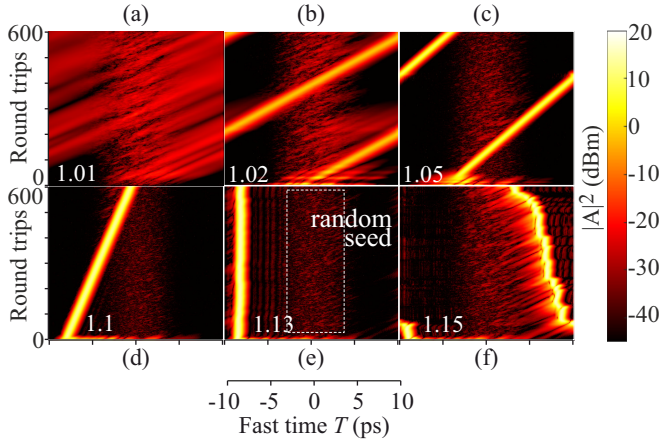


FIG. 4. 2D evolution diagrams of the circulating laser intensity for various normalized pump rates $W_p\tau_{10}$. The corresponding pump rate is noted in each diagram in white. The vertical axis corresponds to the round-trip number while the horizontal axis corresponds to the fast time T . The latter is the same as the moving time-frame T of the NLSE, which is moving with the group velocity v_g . Panel (a) shows no pulse formations, while panels (b)–(e) correspond to the formation and propagation of stable pulses. The random noise seed that simulates spontaneous emission can be seen in all panels around $T = 0$ and is explicitly denoted in panel (e) with the white dashed rectangle. (f) The pulse shows significant changes from round trip to round trip and thus cannot be characterized as stable. Note that the label and units for the horizontal axis are common between all panels and are given below them.

$W_p\tau_{10}$. The peak power can reach tens of milliwatts with increased pumping. Also, the bandwidth quickly reaches the THz range, while the temporal width ranges from about 1 ps to hundreds of femtoseconds. In the leftmost gray area, we did not locate any stable pulse formation. In the rightmost area on the other hand, we did observe the formation of pulses but they did not stabilize within the simulation round trips. To corroborate our stability argument, we present in Fig. 4 the 2D evolution diagrams of the circulating laser intensity for several normalized pump rates. The chosen pump rates directly correspond to some of the points in Fig. 3. We observe that at very low pump rates just above the threshold, Fig. 4(a), no pulse can be formed. By slowly increasing the pump rate [Figs. 4(b)–4(e)], pulses are formed from the injected noise and remain stable through the random perturbations of the continuously generated noisy seed. The latter, which is used to simulate spontaneous emission, can be seen in all of the panels around the $T = 0$ points. The time window corresponds to one round trip. The time instance at which the pulse is present varies depending on the pump rate, where stronger pump rates reduce the speed of the shift. Further increase of the pump rate, Fig. 4(f), leads to pulses that are not stable, since they significantly change from round trip to round trip.

Going back to Fig. 3(c), we observe that for low pumping the time-bandwidth product of the resulting pulses is closer to a transform-limited sech^2 pulse, while for higher pumping it is closer to that of a transform-limited Gaussian pulse. Both of these are known solutions for mode-locked lasers, but the former has specific requirements. The Group Velocity Dispersion

(GVD) and Third Order Dispersion (TOD) parameters at the signal wavelength are calculated to be $1.62 \times 10^{-24} \text{ s}^2/\text{m}$ and $-4.04 \times 10^{-39} \text{ s}^3/\text{m}$, respectively. The Kerr nonlinear parameters due to SRN and graphene are 255 and $-147 \text{ W}^{-1} \text{ m}^{-1}$ [27,35], respectively. Thus, the total Kerr parameter is positive in every region of the cavity. Since we also have normal GVD, the Kerr contributions of SRN and graphene are incompatible with the formation of a solitonlike pulse.

Finally, the stimulated probability at the pump wavelength W_p is used to evaluate the power density needed from the vertical pump $W_p = \frac{1}{2\hbar} T_{2p} \frac{K_p}{2\omega_p} |\mathbf{E}_p|^2$, where K_p is the coupling constant of Eq. (9) at the pump wavelength, $T_{2p} \approx 28.6 \text{ fs}$ is the polarization dephasing time of the pump transition [34], and the intralayer spontaneous emission lifetime is 290 ps [37]. The TMD refractive index at the pump frequency can be calculated by the total surface conductivity at the pump frequency which is reported as $386 - i574 \mu\text{S}$, where the real part accounts for the pump absorption. Using these values, the optical intensity for a cw plane-wave pump for a given $W_p\tau_{10} = 1.1$ is found to be $I_p = |\mathbf{E}_p|^2/2Z_p \approx 0.174 \text{ MW}/\text{cm}^2$, where Z_p is the intrinsic impedance of the bilayer. Note that this optical intensity corresponds to the electric field inside the bilayer. To estimate an upper bound for the power needed from the pump laser we use the power reflection coefficient for a plane wave at normal incidence (found to be 0.52) and arrive to the very modest value of $0.36 \text{ MW}/\text{cm}^2$.

V. CONCLUSIONS

We studied a mode-locked integrated laser based on 2D materials. A graphene monolayer provided the fast saturable absorber and a $\text{MoS}_2/\text{WSe}_2$ bilayer the gain mechanism. We considered external pumping, in the form of vertical plane-wave illumination. The ring laser consisted of an SRN wire waveguide on a silicon oxide substrate. The simulations included a rigorous gain model, able to capture the TMD polarization dynamics, material and waveguide dispersion effects, and Kerr-type nonlinearities from the SRN waveguide and graphene.

We showed that the integrated SRN ring laser based on 2D materials can access a stable mode-locked regime. The photonic structure itself is within standard fabrication limits, and any technological complexity arises from the placement of the 2D materials. The available out-coupled pulses have a peak power of some microwatts and a duration of hundreds of femtoseconds, rendering them suitable for a wide range of applications. Also, the external pump requirements were evaluated to be quite modest, with the required optical intensity being about $0.36 \text{ MW}/\text{cm}^2$. These simulation results were reached from a noiselike initial seed, showing that the laser operation can be self-starting.

ACKNOWLEDGMENTS

The research work was supported by the Hellenic Foundation for Research and Innovation (H.F.R.I.) under the “First Call for H.F.R.I. Research Projects to Support Faculty Members and Researchers and the Procurement of High-Cost Research Equipment Grant” (Project No. HFRI-FM17-2086).

- [1] H. Tang, S. G. Menabde, T. Anwar, J. Kim, M. S. Jang, and G. Tagliabue, *Nanophotonics* **11**, 917 (2022).
- [2] G. Sinatkas, T. Christopoulos, O. Tsilipakos, and E. E. Kriezis, *J. Appl. Phys.* **130**, 010901 (2021).
- [3] J. You, Y. Luo, J. Yang, J. Zhang, K. Yin, K. Wei, X. Zheng, and T. Jiang, *Laser Photonics Rev.* **14**, 2000239 (2020).
- [4] D. J. Blumenthal, R. Heideman, D. Geuzebroek, A. Leinse, and C. Roeloffzen, *Proc. IEEE* **106**, 2209 (2018).
- [5] Y. Zhang, J. Wu, Y. Yang, Y. Qu, H. E. Dirani, R. Crochemore, C. Sciancalepore, P. Demongodin, C. Grillet, C. Monat, B. Jia, and D. J. Moss, *IEEE J. Sel. Top. Quantum Electron.* **29**, 5100413 (2022).
- [6] Y. Zhang, J. Wu, Y. Yang, Y. Qu, L. Jia, H. E. Dirani, S. Kerdales, C. Sciancalepore, P. Demongodin, C. Grillet, C. Monat, B. Jia, and D. J. Moss, *Adv. Mater. Technol.* **8** (2023).
- [7] D.-S. Liu, J. Wu, H. Xu, and Z. Wang, *Adv. Mater.* **33**, 2003733 (2021).
- [8] S. Liu and A. Khope, *J. Semicond.* **42**, 041307 (2021).
- [9] C. Khurmi, N. B. Hébert, W. Q. Zhang, S. A. V. G. Chen, J. Genest, T. M. Monro, and D. G. Lancaster, *Opt. Express* **24**, 27177 (2016).
- [10] E. Thoen, E. Koontz, D. Jones, F. Kartner, E. Ippen, and L. Kolodziejcki, *IEEE Photonics Technol. Lett.* **12**, 149 (2000).
- [11] N. Singh, E. Ippen, and F. X. Kärtner, *Opt. Express* **28**, 22562 (2020).
- [12] S.-L. Chua, B. Zhen, J. Lee, J. Bravo-Abad, O. Shapira, and M. Soljačić, *J. Mater. Chem. C* **2**, 1463 (2014).
- [13] D. Korn, M. Lauermann, S. Koeber, P. Appel, L. Alloatti, R. Palmer, P. Dumon, W. Freude, J. Leuthold, and C. Koos, *Nat. Commun.* **7**, 10864 (2016).
- [14] D. Kohler, I. Allegro, S. F. Wondimu, L. Hahn, W. Freude, and C. Koos, *Opt. Express* **28**, 5085 (2020).
- [15] Y. Li, J. Zhang, D. Huang, H. Sun, F. Fan, J. Feng, Z. Wang, and C. Z. Ning, *Nat. Nanotechnol.* **12**, 987 (2017).
- [16] Y. Ye, Z. J. Wong, X. Lu, X. Ni, H. Zhu, X. Chen, Y. Wang, and X. Zhang, *Nat. Photonics* **9**, 733 (2015).
- [17] P. Rivera, H. Yu, K. L. Seyler, N. P. Wilson, W. Yao, and X. Xu, *Nat. Nanotechnol.* **13**, 1004 (2018).
- [18] O. Karni, E. Barré, S. C. Lau, R. Gillen, E. Y. Ma, B. Kim, K. Watanabe, T. Taniguchi, J. Maultzsch, K. Barmak, R. H. Page, and T. F. Heinz, *Phys. Rev. Lett.* **123**, 247402 (2019).
- [19] G. Nousios, T. Christopoulos, O. Tsilipakos, and E. E. Kriezis, *Phys. Rev. Appl.* **19**, 064027 (2023).
- [20] Y. Liu, H. Fang, A. Rasmita, Y. Zhou, J. Li, T. Yu, Q. Xiong, N. Zheludev, J. Liu, and W. Gao, *Sci. Adv.* **5**, eaav4506 (2019).
- [21] E. Y. Paik, L. Zhang, G. W. Burg, R. Gogna, E. Tutuc, and H. Deng, *Nature (London)* **576**, 80 (2019).
- [22] R.-M. Ma and R. F. Oulton, *Nat. Nanotechnol.* **14**, 12 (2019).
- [23] Y. Kominis, A. Bountis, and V. Kovanis, *J. Appl. Phys.* **127**, 083103 (2020).
- [24] F. Bonaccorso, Z. Sun, T. Hasan, and A. C. Ferrari, *Nat. Photonics* **4**, 611 (2010).
- [25] H.-L. Liu, C.-C. Shen, S.-H. Su, C.-L. Hsu, M.-Y. Li, and L.-J. Li, *Appl. Phys. Lett.* **105**, 201905 (2014).
- [26] C. Hsu, R. Frisenda, R. Schmidt, A. Arora, S. M. Vasconcellos, R. Bratschitsch, H. S. J. Zant, and A. Castellanos-Gomez, *Adv. Opt. Mater.* **7**, 1900239 (2019).
- [27] D. Chatzidimitriou, A. Ptilakis, and E. E. Kriezis, *J. Appl. Phys.* **118**, 023105 (2015).
- [28] C. Errando-Herranz, E. Schöll, R. Picard, M. Laini, S. Gyger, A. W. Elshaari, A. Branny, U. Wennberg, S. Barbat, T. Renaud, M. Sartison, M. Brotons-Gisbert, C. Bonato, B. D. Gerardot, V. Zwiller, and K. D. Jöns, *ACS Photonics* **8**, 1069 (2021).
- [29] C. Jin, E. Y. Ma, O. Karni, E. C. Regan, F. Wang, and T. F. Heinz, *Nat. Nanotechnol.* **13**, 994 (2018).
- [30] C. Javerzac-Galy, A. Kumar, R. D. Schilling, N. Piro, S. Khorasani, M. Barbone, I. Goykhman, J. B. Khurgin, A. C. Ferrari, and T. J. Kippenberg, *Nano Lett.* **18**, 3138 (2018).
- [31] D. Chatzidimitriou and E. E. Kriezis, *Phys. Rev. A* **102**, 053512 (2020).
- [32] A. E. Siegman, *Lasers* (University Science Books, Melville, NY, USA, 1986).
- [33] S.-L. Chua, Y. Chong, A. D. Stone, M. Soljačić, and J. Bravo-Abad, *Opt. Express* **19**, 1539 (2011).
- [34] G. Moody, C. K. Dass, K. Hao, C.-H. Chen, L.-J. Li, A. Singh, K. Tran, G. Clark, X. Xu, G. Berghäuser, E. Malic, A. Knorr, and X. Li, *Nat. Commun.* **6**, 8315 (2015).
- [35] T. Wang, D. K. T. Ng, S.-K. Ng, Y.-T. Toh, A. K. L. Chee, G. F. R. Chen, Q. Wang, and D. T. H. Tan, *Laser Photonics Rev.* **9**, 498 (2015).
- [36] T. Hansson and S. Wabnitz, *J. Opt. Soc. Am. B* **32**, 1259 (2015).
- [37] M. Palumbo, M. Bernardi, and J. C. Grossman, *Nano Lett.* **15**, 2794 (2015).